Properties of the rotational bands in ^{161}Er

L. Chen,[1,2] X. H. Zhou,[1,2,*] Y. H. Zhang,[1] Y. Zheng,[1] M. L. Liu,[1] S. T. Wang,[1,2] F. Ma,[1] N. T. Zhang,[1,2] Y. D. Fang,[1] W. Hua,[1] S. Guo,[1] Y. H. Qiang,[1] H. B. Zhou,[1,2] G. S. Li,[1,2] H. X. Wang,[1,2] B. Ding,[1,2] X. G. Lei,[1] Y. X. Guo,[1] L. H. Zhu,[3] X. G. Wu,[3] S. Q. Zhang,[4] and J. Meng[4]

[1]*Institute of Modern Physics, Chinese Academy of Sciences, Lanzhou 730000, China*

[2]*Graduate University of Chinese Academy of Sciences, Beijing 100049, China*

[3]*China Institute of Atomic Energy, Beijing 102413, China*

[4]*School of Physics, and State-Key Laboratory Nuclear Physics & Technology, Peking University, Beijing 100871, China*

(Received 13 September 2010; revised manuscript received 16 February 2011; published 22 March 2011)

High-spin states in ^{161}Er have been studied experimentally using the ^{150}Nd(^{16}O,5n) reaction at a beam energy of 86 MeV. The $5/2^+[642]$, $3/2^-[521]$, and $11/2^-[505]$ bands are extended up to high-spin states, and particularly the $\alpha = -1/2$ branch of the ground state $3/2^-[521]$ band is revised significantly. The relatively enhanced $E1$ transitions from the $3/2^-[521]$ band to the $5/2^+[642]$ band are observed. The band properties are analyzed within the framework of a triaxial particle-rotor model, and near-prolate shape and triaxial deformation are proposed to the $3/2^-[521]$ and $5/2^+[642]$ bands, respectively. Signature inversion occurs in the $3/2^-[521]$ band after the band crossing in ^{161}Er, and the systematics of the signature inversion associated with the $3/2^-[521]$ configuration are discussed. By analyzing the properties of the relatively enhanced $E1$ transitions, it is found that the $R(E1/E2)$ values show angular momentum dependence before the band crossing, and these enhanced $E1$ transitions could be attributed to octupole softness.

DOI: 10.1103/PhysRevC.83.034318 PACS number(s): 21.10.Re, 23.20.Lv, 21.60.Ev, 27.70.+q

I. INTRODUCTION

In the well-deformed 160 mass region, the properties of rotational bands in nuclei have been studied extensively [1–11]. In the odd-N nuclei with a prolate deformation, the neutron Fermi surface is located at the $i_{13/2}$, $h_{9/2}$, $f_{7/2}$, and $h_{11/2}$ subshells, and variant types of rotational bands were observed experimentally [1–8]. These bands exhibit interesting large signature splitting, anomalous band-crossing frequency, and signature inversion, among which the mechanism of signature inversion after band crossing in the odd-N nuclei was not well understood [3,6–8]. Signature quantum number α, describing the invariance of the intrinsic Hamiltonian of an axially deformed nucleus with respect to 180° rotation around a principal axis, is a conserved quantum number [12,13]. The signature splitting is defined as the difference in energies at a given rotational frequency for the pair of signature partners. For a nuclear system with an odd particle number, the favored signature defined by $\alpha_f = 1/2 \times (-1)^{j-1/2}$ is usually lower in energy with respect to the unfavored one $\alpha_{\rm uf} = 1/2 \times (-1)^{j+1/2}$, where j is the angular momentum of the subshell associated with the odd particle. However, this rule is broken in some odd-A nuclei [3,6–8,13–15]; the expected favored branch lies higher in energy than the unfavored one after the first band crossing. This phenomenon is known as the signature inversion [13]. Great efforts have been devoted to the understanding of signature inversion mechanisms, and the nuclear triaxiality, band crossing, and shape change have been proposed as possible reasons [13,16,17]. The signature inversion in the $3/2^-[521]$ band was observed in the isotones ^{163}Yb [7] and ^{159}Dy [8], and the isotopes ^{159}Er [6] and ^{163}Er [3] of ^{161}Er. Therefore, it is important to search for the signature inversion in ^{161}Er, and systematically analyze this phenomenon.

In this mass region, another interesting phenomenon concerns the occurrence of enhanced $E1$ transitions between two bands with opposite parities. Generally, low-energy $E1$ transitions observed in nuclei are strongly hindered [9], and the observed $B(E1)$ rates are typically 10^{-6} Weisskopf unit. However, relatively enhanced $E1$ transitions with strength larger than 10^{-4} as compared with the single-particle estimation were observed experimentally between two rotational bands with opposite parities in nuclei [18]. The octupole softness or deformation together with quadrupole deformation could lead to an enhanced dipole moment, which was suggested by Strutinsky [19] and Bohr and Mottelson [20]. In the presence of octupole deformation, a dipole moment is produced in the intrinsic system because of a shift between the mass center of nucleus and the center of electric charge [20]. It is well known that nuclei in the light Ra-Th [21,22] and heavy Ba-Sm [23,24] regions exhibit the strong $E1$ transitions, which are attributed to a static octupole deformation [18]. On the other hand, relatively strong $E1$ transitions between two rotational bands in the rare-rarth nuclei were also reported [11,18]. Hamamoto *et al.* [9–11] systematically analyzed the low-energy $E1$ transitions in this region, and pointed out that these $E1$ transitions could be explained by taking into account the effect of the particle-octupole-vibration coupling. The $E1$ transitions connecting the pair of the $3/2^-[521]$ and $5/2^+[642]$ bands in nuclei with neutron number around 93 were expected to be enhanced [9]. In fact, a number of relatively enhanced $E1$ transitions were observed in the ^{163}Yb [7], ^{159}Dy [8], and ^{157}Gd [25] isotones of ^{161}Er. Therefore, it is very interesting to search for the analogous $E1$ transitions in ^{161}Er with $N = 93$.

*zxh@impcas.ac.cn

Prior to this work, detailed knowledge of low-spin states in ^{161}Er was provided from decay studies of ^{161}Tm [26]. Based on the α-induced reaction and ^{150}Nd (^{16}O,5n) reaction [1,2], rotational bands associated with the $5/2^+[642]$, $3/2^-[521]$, and $11/2^-[505]$ configurations were established in ^{161}Er. Garrett *et al.* proposed the latest medium- to high-spin level scheme for ^{161}Er in print [1]. Additionally, rotational bands in ^{161}Er were extended to very high spins using the ^{130}Te (^{36}S,5n) reaction [27,28]. In this article we revise the $\alpha = -1/2$ branch of the $3/2^-[521]$ band reported previously [1], and report the relatively enhanced $E1$ transitions from the $3/2^-[521]$ band to the $5/2^+[642]$ band. The experimental details and data analysis are described in Sec. II, and the experimental results are given. The brief introduction on the triaxial particle-rotor model is presented in Sec. III. In Sec. IV, band properties of the crossing frequencies, alignment gain, signature splitting, signature inversion, and occurrence of the enhanced $E1$ transitions are discussed. Concluding remarks are presented in Sec. V.

II. EXPERIMENTS AND RESULTS

A. Measurements

The high-spin states in ^{161}Er were populated via the ^{150}Nd (^{16}O,5n) reaction. The ^{16}O beam was provided by the HI-13 Tandem Accelerator at China Institute of Atomic Energy in Beijing (CIAE). The target was a 1.5 mg/cm^2 foil of ^{150}Nd (isotopically enriched to 94.2%) with a 10.8 mg/cm^2 Pb backing to stop the recoiling nuclei. The measurements were performed with a detector array, which consisted of nine HPGe detectors with BGO anti-Compton (AC) shields, two low-energy planar HPGe detectors, and one Clover detector. The nine HPGe detectors had an efficiency of 30% each; the planar detector had 20%, and the Clover detector had 160% relative to $3''\times3''$ NaI. The BGO shield had a suppression factor of about 3.5, which was measured with a ^{60}Co source. The suppression factor was defined as the ratio of counts in the energy region of 400∼900 keV in properly normalized unsuppressed and suppressed spectra. Of the nine HPGe detectors, five were placed at $\pm42^\circ$, one at 65°, and three at 90° with respect to the beam direction. The Clover detector was mounted at 90°, and the planar detectors were at 130° with respect to the beam direction. Lead collimators were placed in front of the HPGe detectors. To suppress the huge x-ray peaks of Nd and Pb, copper absorbers of 0.5-mm thickness were placed in front of the nine HPGe detectors, and 0.2-mm copper absorbers were used for the planar detectors and clover detector. The thick absorbers prohibited us from observing low-energy γ rays. The detectors were calibrated with standard ^{133}Ba and ^{152}Eu sources; the typical energy resolution was 2.0∼3.0 keV at full width at half maximum for the 1332.5-keV line from ^{60}Co. The relatively poor energy resolution was mainly caused by the neutron damage of the Ge detectors. X-γ-t and γ-γ-t coincidence measurements were carried out at a beam energy of 86 MeV, at which energy the yield of ^{161}Er was found to be large [1]. Here, t refers to the relative time difference between any two coincident γ rays detected within ±200 ns. Because of the location of the compound nucleus ^{166}Er in the proximity of the stability line, neutron evaporation channels were dominant for the present projectile and target combination. The main products were ^{161}Er, ^{160}Er, and ^{162}Er nuclei, among which the ^{161}Er nuclide had the largest yield. A total of 9.1×10^7 γ-γ coincidence events were recorded in experiment. After gain matching, these data were sorted into a $4k \times 4k$ symmetric E_γ-E_γ matrix for off-line analysis.

To obtain multipolarity information for γ rays deexciting the oriented states, the coincidence data were sorted into two asymmetric matrices whose x axis is the γ-ray energy deposited in the detectors at any angles, and y axis is the γ-ray energy deposited in the detectors at $\pm42^\circ$ and 90°, respectively. By gating on the x axis with suitable γ rays, two spectra measured at $\pm42^\circ$ and 90° angle positions were obtained. After correcting for the overall detection efficiency of the detectors at each of the two angles and normalizing the two spectra with respect to each other, γ-ray anisotropy [$R_{\rm ADO}(\gamma)$] was deduced from the intensity ratio in the two spectra. Typical γ-ray anisotropies for the known γ rays observed in this experiment are 1.4 for stretched quadrupole transitions and 0.7 for stretched pure dipole transitions. Therefore, we have assigned the stretched quadrupole transition and stretched dipole transition to the γ rays of ^{161}Er with anisotropies around 1.4 and 0.7, respectively.

B. Level scheme

In the previous work, many low-lying states in ^{161}Er were identified from the decay studies of ^{161}Tm [26], and rotational bands were established using the in-beam spectroscopic techniques [1,2]. This provides important basis for the present work. Assignments of the observed new γ rays to ^{161}Er were based on the coincidences with the known γ rays [1,2]. Gated spectrum was produced for each of the γ rays assigned to ^{161}Er. Based on the analysis of γ-γ coincidence relationships, a new level scheme for ^{161}Er was proposed and presented in Fig. 1. The low-lying transitions identified in the decay work are also shown for completeness in Fig. 1 [26]. The ordering of transitions in the level scheme was determined according to the γ-ray relative intensities, γ-γ coincidence relationships, and γ-ray energy sums. The transition character was deduced from the measured $R_{\rm ADO}$ results. In assigning spins and parities to the levels observed, $E2$ multipolarity is assumed for stretched quadrupole transitions. $E1$ or $M1$ character is possible for the dipole transitions. $M1$ transitions may have $E2$ admixtures. Such an admixture is neglected in the present work as is the possibility of pure, unstretched transitions. The spins and parities for the known states were adopted from the previous work [1,2], and these values were used as the references for the spin and parity assignments to the high-spin states. In the present work, we have used the general yrast argument that levels populated in heavy-ion reactions usually have spins increasing with increasing excitation energy. Therefore, the measured γ-ray anisotropy results allow straightforward determinations of spins and parities for the excited states in ^{161}Er. Some brief explanations of the level scheme are given as follows.

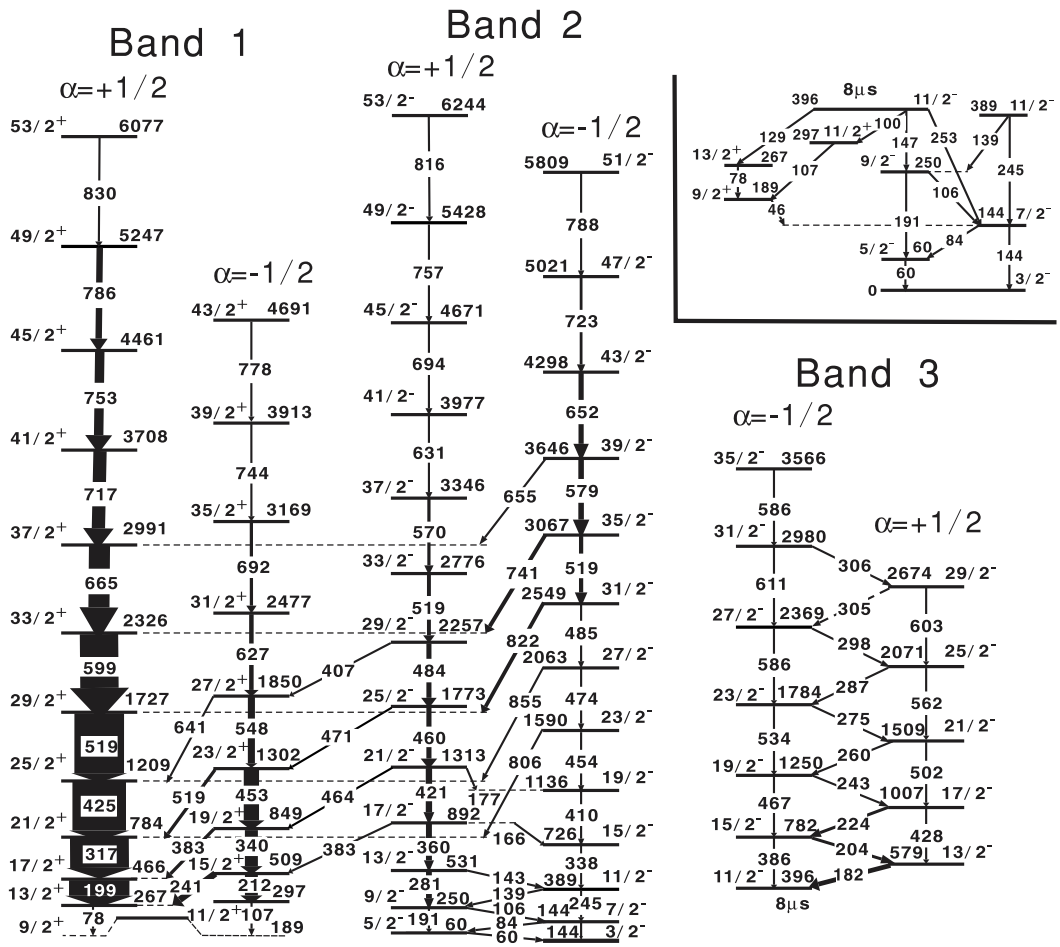

FIG. 1. Level scheme of ^{161}Er deduced from the present work. The widths of the arrows indicate the relative transition intensities. The low-spin transitions identified in decay work [26] are shown in the top right corner. The labeling of individual $E2$ sequences by signature exponents serves the discussion in the text.

Band 1 was most strongly populated. This band was observed previously, and suggested to be associated with the $i_{13/2}$ configuration [1,2]. The present work has confirmed the results reported [1,2]. The spectra gated on the 627.1- and 665.4-keV transitions are presented in Fig. 2.

Band 2 was proposed to be associated with the $3/2^{-}[521]$ ground state [1,2]. The γ-ray spectra gated on the 821.5-, 570.2-, 651.8-, 244.7-, and 165.5-keV transitions are shown in Fig. 3. In the spectrum gated on the 165.5-keV transition, the 136.5-, 193.5-, and 415.0-keV lines come from Coulomb excitation of ^{181}Ta, which is the target holder. With the existence of interband and intraband transitions, the positions of many transitions in the level scheme are rather firm in the level scheme. For example, the 651.8-keV transition is in coincidence with the 654.6-, 740.9-, 821.5-, and 854.5-keV interband transitions. The 654.6-keV transition shows coincidence with the 198.7-, 317.4-, 425.0-, 518.5-, 598.9-, and 665.4-keV transitions in Band 1, the 740.9-keV transition in coincidence with the 198.7-, 317.4-, 425.0-, 518.5-, and 598.9-keV transitions, the 821.5-keV transition in coincidence with the 198.7-, 317.4-, 425.0-, and 518.5-keV transitions, and the 854.5-keV transition in coincidence with the 198.7-, 317.4-, and 425.0-keV transitions. These coincidence patterns, together with energy sum relationships of the involved transitions, firmly established the locations of the 654.6-, 740.9-, 821.5-, and 854.5-keV interband transitions

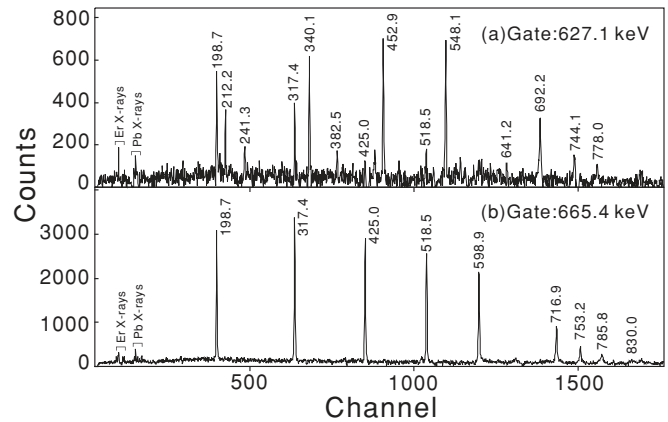

FIG. 2. The γ-ray spectra gated on the 627.1- and 665.4-keV transitions. They are representative for band 1. The Pb x rays are attributed to unwanted excitations of the collimator material (see text).

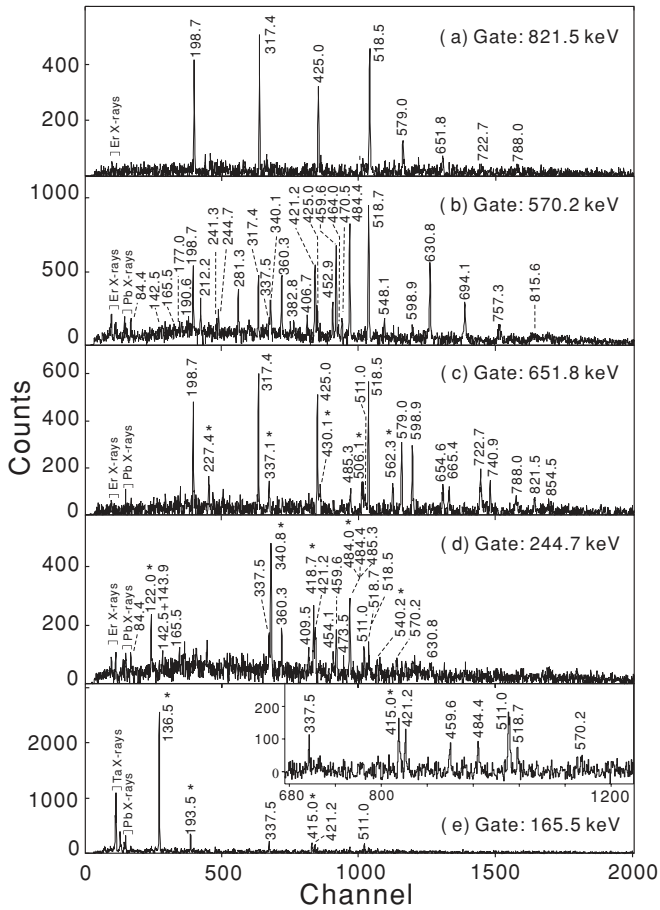

FIG. 3. The γ-ray spectra gated on the (a) 821.5-keV transition, (b) 570.2-keV transition, (c) 651.8-keV transition, (d) 244.7-keV transition, and (e) 165.5-keV transition. They show the existence of band 2 and the interband transitions. In panel (a), there is a 518.5-keV double line. In panel (c), the asterisks indicate the contaminations mainly from ^{162}Er. In panel (d), the asterisks denote peaks from the ground-state band of ^{152}Sm, which was produced via the two-proton transfer reaction on the ^{150}Nd target. In panel (e), the transitions labeled by the asterisks come from Coulomb excitation of ^{181}Ta, which is the target holder.

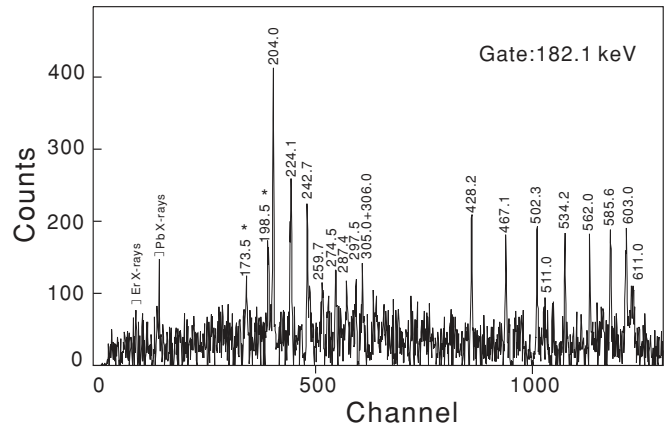

FIG. 4. The γ-ray spectrum gated on the 182.1-keV transition. It is representative for band 3. The 173.5- and 198.5-keV transitions might belong to ^{161}Er, but they are too weak to be placed into the level scheme.

in the level scheme, and also fixed the transition order of the 485.3-, 518.5-, 579.0-, and 651.8-keV transitions. The $\alpha = +1/2$ branch is extended up to $I^{\pi} = 53/2^{-}$ state. Four interband $E1$ transitions of 382.8, 464.0, 470.5, and 406.7 keV, which link the $\alpha = +1/2$ sequence in band 2 and the $\alpha = -1/2$ sequence in band 1, are observed. Transitions between the two signatures are only observed at the bottom of band 2. In the previous work [1], it was proposed that the low-lying $\alpha = -1/2$ branch of band 2 consists of the 244.7-, 340.8-, 418.7-, and 484.0-keV transitions. However, this cascade should be attributed to the ground-state band of ^{152}Sm [29], which was produced via the two-proton transfer exit channel. Because the medium-lying levels in the $\alpha = -1/2$ branch mainly decay to band 1, the low-lying levels are weakly populated. As shown in Fig. 3, the spectra gated on the 244.7- and 165.5-keV transitions display the existence of the low-lying levels in the $\alpha = -1/2$ branch. The 165.5-keV transition is in coincidence with the 337.5- and 421.2-keV transitions but not with the 360.3- and 409.5-keV transitions. The 244.7-keV transition shows coincidence with the 337.5, 409.5, 454.1, and 473.5 transitions. On the basis of analysis of the coincidence and energy sum relationships of the transitions involved, we have determined that the $\alpha = -1/2$ branch is composed of the 143.9-, 244.7-, 337.5-, 409.5-, 454.1-, 473.5-, 485.3-, 518.5-, 579.0-, 651.8-, 722.7-, and 788.0-keV transitions.

Band 3 has a typical character of coupled band. This band was associated with the $11/2^{-}[505]$ configuration, and was known up to the $27/2^{-}$ and $29/2^{-}$ states in the previous work [1]. The present work has extended the $\alpha = -1/2$ branch of band 3 from $I^{\pi} = 27/2^{-}$ to $I^{\pi} = 35/2^{-}$. We have to point out that the 585.6-keV transition is a double line. The ordering of the high-lying transitions is rather certain because of the observation of the 287.4-, 297.5-, and 306.0-keV intraband transitions. A γ-ray spectrum gated on the 182.1-keV transition is shown in Fig. 4.

C. Experimental $E1$ transition probabilities

As shown in Fig. 1, several pronounced $E1$ transitions are observed between the bands built on the $3/2^{-}[521]$ and $5/2^{+}[642]$ configurations. For the $\Delta I = 1$ transitions between these bands, the branching ratios, which are defined as

$$\lambda = \frac{T_{\gamma}(I \rightarrow I-2)}{T_{\gamma}(I \rightarrow I-1)}, \tag{1}$$

were extracted for most transitions. Here $T_{\gamma}(I \rightarrow I-2)$ and $T_{\gamma}(I \rightarrow I-1)$ are the γ-ray intensities of the $E2$ and $E1$ transitions, respectively. These intensities are measured in a summed coincidence spectrum gated by the transitions above the state of interest. The experimental $B(E1)/B(E2)$ ratios are extracted from the relative γ-ray intensities using the following

formula,

$$\frac{B(E1;I\to I-1)}{B(E2;I\to I-2)} = 0.771\times\frac{[E_\gamma(I\to I-2)]^5}{[E_\gamma(I\to I-1)]^3} \times\frac{1}{\lambda}(10^{-6}\mathrm{fm}^{-2}), \quad (2)$$

where E_γ is measured in MeV.

The relative intensities for some strong γ rays are measured in the total projection spectrum. Most of the relative intensities are extracted from the spectra gated on the bottom transitions in the band. The relative intensities are corrected with the detection efficiencies. The γ-ray energies, spin and parity assignments, relative γ-ray intensities, level energies, branching ratios λ, extracted $B(E1)/B(E2)$ values, and anisotropies R_{ADO} are presented in Table I grouped in sequences for each band.

III. THEORETICAL CALCULATIONS

Various models have been developed to study the properties of rotational bands in odd-A nuclei [2,13,16,17,30,31], among which the triaxial particle-rotor model (PRM) is widely used [2,16,17,31]. Qi *et al.* revised the PRM, and successfully interpreted the signature splitting in ^{173}W [31]. In the present work, we will apply the PRM to discuss the rotational band properties in ^{161}Er.

The Hamiltonian of an odd-A nucleus can be expressed as [12]

$$\hat{H} = \hat{H}_{\mathrm{rot}} + \hat{H}_{\mathrm{intr}}, \quad (3)$$

where $\hat{H}_{\mathrm{rot}}$ represents the Hamiltonian of the triaxial rotor,

$$\hat{H}_{\mathrm{rot}} = \sum_{i=1}^{3}\frac{\hat{\Re}_i^2}{2\Im_i} = \sum_{i=1}^{3}\frac{(\hat{I}_i-\hat{j}_i)^2}{2\Im_i}, \quad (i=1,2,3). \quad (4)$$

Here, $\hat{\Re}_i$, $\hat{I}_i$, and $\hat{j}_i$ are the angular momentum operators for the core, nucleus, and valence nucleon, respectively. The moments of inertia for irrotational flow $\Im_i$ are adopted; that is,

$$\Im_i = \frac{4}{3}\Im_0(I)\sin^2\left(\gamma+\frac{2\pi}{3}i\right), \quad (i=1,2,3), \quad (5)$$

where $\Im_0$ is the variable moment of inertia of the core, and it depends on the quadrupole deformation ε_2 and the nuclear mass A [32]. γ denotes the degree of triaxiality.

$\hat{H}_{\mathrm{intr}}$ is the intrinsic Hamiltonian for valence nucleon including the Hamiltonian of the unpaired single particle $\hat{H}_{\mathrm{sp}}$ and pairing correlation $\hat{H}_{\mathrm{pair}}$,

$$\hat{H}_{\mathrm{intr}} = \hat{H}_{\mathrm{sp}} + \hat{H}_{\mathrm{pair}}. \quad (6)$$

Similar to Ref. [33], the Nilsson type single-particle Hamiltonian is employed:

$$\hat{H}_{\mathrm{sp}} = \left(\frac{p^2}{2m}+\frac{1}{2}m\omega_0^2\rho^2\right) - \frac{2}{3}\varepsilon_2\sqrt{\frac{4\pi}{5}}\hbar\omega_0\rho^2 \times\left[\cos\gamma Y_{20}+\frac{1}{\sqrt{2}}\sin\gamma(Y_{22}+Y_{2-2})\right] -\kappa\hbar\omega_0\{2\vec{l}\cdot\vec{s}+\mu(\vec{l}^2-\langle\vec{l}^2\rangle_N\}, \quad (7)$$

where κ and μ are the Nilsson parameters, and they depend on the main oscillator quantum number N [34].

Therefore, the single-particle states are obtained by diagonalizing the Hamiltonian $\hat{H}_{\mathrm{sp}}$, and can be written as

$$a_\nu^+|0\rangle = \sum_{Nlj\Omega} c^{(\nu)}_{Nlj\Omega}|Nlj\Omega\rangle,$$
$$a_{\bar{\nu}}^+|0\rangle = \sum_{Nlj\Omega}(-1)^{j-\Omega}c^{(\nu)}_{Nlj\Omega}|Nlj-\Omega\rangle, \quad (8)$$

where Ω is the projection of the single-particle angular momentum $\hat{j}$ on the third axis.

To obtain the PRM solutions, the total Hamiltonian in Eq. (4) must be diagonalized in a complete basis space. When pairing correlations are neglected, one can construct the so-called strong coupling basis as

$$|IMK\nu\rangle = \sqrt{\frac{1}{2}}\sqrt{\frac{2I+1}{8\pi^2}} \times\left[D^I_{M,K}a_\nu^+|0\rangle+(-1)^{I-K}D^I_{M,-K}a_{\bar{\nu}}^+|0\rangle\right], \quad (9)$$
$$K = \cdots,-7/2,-3/2,+1/2,+5/2,\cdots$$

where $D^I_{M,K}$ is the rotational matrix, and K is the projection of total angular momentum I on the intrinsic quantisation axis.

When pairing effects are included in the PRM, one should replace the single-particle state $a_\nu^+|0\rangle$ in the basis states with the standard BCS quasiparticle state $\alpha_\nu^+|\tilde{0}\rangle$ to obtain a new expansion basis, where $|\tilde{0}\rangle$ is the standard BCS vacuum state. Meanwhile, the single-particle energies ε_ν should be replaced by quasiparticle energies,

$$E_\nu = \sqrt{(\varepsilon_\nu-\lambda)^2+\Delta^2}, \quad (10)$$

where λ denotes the Fermi energy, and Δ is the pairing-gap parameter.

By diagonalization in this new basis, we get the solution of the PRM; namely, the level energies which could be compared with the experimental data, as well as the wave functions which are written as

$$|IM\rangle = \sum_{K,\nu}C_\nu^{IK}|IMK\nu\rangle. \quad (11)$$

The detailed description for the revised PRM can be found in Ref. [31].

IV. DISCUSSION

A. Alignment properties

The odd-A nucleus ^{161}Er with $Z=68$ and $N=93$ is located in the well-deformed region, and consequently exhibits a typical rotational character [1,2]. At a large prolate deformation, the Nilsson orbits near the neutron Fermi surface are $5/2^+[642]$, $3/2^+[651]$, $3/2^-[521]$, $5/2^-[523]$, and $11/2^-[505]$, which originate from the $i_{13/2}$, $h_{9/2}$, $f_{7/2}$, and $h_{11/2}$ subshells, respectively. To discuss the band properties at high spin and study the effect of rotation on the independent particle motion in a deformed potential, it is necessary to

TABLE I. γ-ray transition energies, spin and parity assignments, γ-ray intensities, branching ratios, $B(E1)/B(E2)$ values, and ADO ratios in ^{161}Er.

$E\gamma$(keV)[a]	$J_i^\pi \rightarrow J_f^\pi$[b]	I_γ[c]	λ[d]	$\frac{B(E1)}{B(E2)}(10^{-6}\mathrm{fm}^{-2})$	R_{ADO}	E_i(keV)[e]
Band 1						
78.0	$\frac{13}{2}^+ \rightarrow \frac{9}{2}^+$	$\geqslant$42				267.4
198.7	$\frac{17}{2}^+ \rightarrow \frac{13}{2}^+$	1000			1.65(22)	466.1
317.4	$\frac{21}{2}^+ \rightarrow \frac{17}{2}^+$	974			1.69(15)	783.5
425.0	$\frac{25}{2}^+ \rightarrow \frac{21}{2}^+$	887			1.47(14)	1208.5
518.5	$\frac{29}{2}^+ \rightarrow \frac{25}{2}^+$	$\geqslant$822			1.32(13)	1727.0
598.9	$\frac{33}{2}^+ \rightarrow \frac{29}{2}^+$	635			1.27(18)	2325.9
665.4	$\frac{37}{2}^+ \rightarrow \frac{33}{2}^+$	349			1.35(16)	2991.3
716.9	$\frac{41}{2}^+ \rightarrow \frac{37}{2}^+$	220			1.29(26)	3708.2
753.2	$\frac{45}{2}^+ \rightarrow \frac{41}{2}^+$	156			1.41(24)	4461.4
785.8	$\frac{49}{2}^+ \rightarrow \frac{45}{2}^+$	106			1.41(24)	5247.2
830.0	$\frac{53}{2}^+ \rightarrow \frac{49}{2}^+$	31			0.97(55)	6077.2
212.2	$\frac{15}{2}^+ \rightarrow \frac{11}{2}^+$	214			1.51(24)	508.8
340.1	$\frac{19}{2}^+ \rightarrow \frac{15}{2}^+$	215			1.49(14)	848.9
452.9	$\frac{23}{2}^+ \rightarrow \frac{19}{2}^+$	253			1.51(22)	1301.8
548.1	$\frac{27}{2}^+ \rightarrow \frac{23}{2}^+$	117			1.55(25)	1849.9
627.1	$\frac{31}{2}^+ \rightarrow \frac{27}{2}^+$	74			1.49(22)	2477.0
692.2	$\frac{35}{2}^+ \rightarrow \frac{31}{2}^+$	54			1.26(27)	3169.2
744.1	$\frac{39}{2}^+ \rightarrow \frac{35}{2}^+$	33			1.15(26)	3913.3
778.0	$\frac{43}{2}^+ \rightarrow \frac{39}{2}^+$	29			1.87(67)	4691.3
107.2	$\frac{11}{2}^+ \rightarrow \frac{9}{2}^+$	$\geqslant$7				296.6
241.3	$\frac{15}{2}^+ \rightarrow \frac{13}{2}^+$	110			0.64(11)	508.8
382.5	$\frac{19}{2}^+ \rightarrow \frac{15}{2}^+$	55			0.57(11)	848.9
518.5	$\frac{23}{2}^+ \rightarrow \frac{21}{2}^+$	55			0.83(16)	1301.8
641.2	$\frac{27}{2}^+ \rightarrow \frac{25}{2}^+$	10			0.57(31)	1849.9
Band 2						
143.9	$\frac{7}{2}^- \rightarrow \frac{3}{2}^-$	$\geqslant$19				143.9
244.7	$\frac{11}{2}^- \rightarrow \frac{7}{2}^-$	$\geqslant$34			1.49(27)	388.6
337.5	$\frac{15}{2}^- \rightarrow \frac{11}{2}^-$	33			1.73(47)	726.1
409.5	$\frac{19}{2}^- \rightarrow \frac{15}{2}^-$	25			1.03(22)	1135.6
454.1	$\frac{23}{2}^- \rightarrow \frac{19}{2}^-$	15			1.04(46)	1589.7
473.5	$\frac{27}{2}^- \rightarrow \frac{23}{2}^-$	21			1.71(74)	2063.2
485.3	$\frac{31}{2}^- \rightarrow \frac{27}{2}^-$	32			1.27(25)	2548.5
518.5	$\frac{35}{2}^- \rightarrow \frac{31}{2}^-$	70			1.58(29)	3067.0
579.0	$\frac{39}{2}^- \rightarrow \frac{35}{2}^-$	92			1.71(41)	3646.0
651.8	$\frac{43}{2}^- \rightarrow \frac{39}{2}^-$	86			1.11(25)	4297.8
722.7	$\frac{47}{2}^- \rightarrow \frac{43}{2}^-$	46			1.13(23)	5020.5
788.0	$\frac{51}{2}^- \rightarrow \frac{47}{2}^-$	25				5808.5
190.6	$\frac{9}{2}^- \rightarrow \frac{5}{2}^-$	$\geqslant$27			1.83(79)	250.1
281.3	$\frac{13}{2}^- \rightarrow \frac{9}{2}^-$	96			1.79(20)	531.4
360.3	$\frac{17}{2}^- \rightarrow \frac{13}{2}^-$	98			1.57(22)	891.7
421.2	$\frac{21}{2}^- \rightarrow \frac{17}{2}^-$	105			1.45(17)	1312.9
459.6	$\frac{25}{2}^- \rightarrow \frac{21}{2}^-$	85			1.57(18)	1772.5
484.4	$\frac{29}{2}^- \rightarrow \frac{25}{2}^-$	84			1.51(21)	2256.9
518.7	$\frac{33}{2}^- \rightarrow \frac{29}{2}^-$	65			1.44(31)	2775.6
570.2	$\frac{37}{2}^- \rightarrow \frac{33}{2}^-$	53			1.43(23)	3345.8
630.8	$\frac{41}{2}^- \rightarrow \frac{37}{2}^-$	33			1.50(41)	3976.6
694.1	$\frac{45}{2}^- \rightarrow \frac{41}{2}^-$	17			1.20(37)	4670.7
757.3	$\frac{49}{2}^- \rightarrow \frac{45}{2}^-$	6			1.79(66)	5428.0
815.6	$\frac{53}{2}^- \rightarrow \frac{49}{2}^-$	3				6243.6

TABLE I. *(Continued.)*

$E\gamma$(keV)[a]	$J_i^\pi \rightarrow J_f^\pi$[b]	I_γ[c]	λ[d]	$\frac{B(E1)}{B(E2)}(10^{-6}\mathrm{fm}^{-2})$	R_{ADO}	E_i(keV)[e]
106.2	$\frac{9}{2}^- \rightarrow \frac{7}{2}^-$	$\geqslant 3$				250.1
138.7	$\frac{11}{2}^- \rightarrow \frac{9}{2}^-$	$\geqslant 5$				388.6
142.5	$\frac{13}{2}^- \rightarrow \frac{11}{2}^-$	16				531.4
165.5	$\frac{17}{2}^- \rightarrow \frac{15}{2}^-$	7				891.7
177.0	$\frac{21}{2}^- \rightarrow \frac{19}{2}^-$	5				1312.9
382.8	$\frac{17}{2}^- \rightarrow \frac{15}{2}^+$	13	8.92(13)	0.009(1)	0.79(33)	891.7
464.0	$\frac{21}{2}^- \rightarrow \frac{19}{2}^+$	31	5.85(22)	0.017(4)	0.61(17)	1312.9
470.5	$\frac{25}{2}^- \rightarrow \frac{23}{2}^+$	19	5.22(11)	0.029(3)	0.94(17)	1772.5
406.7	$\frac{29}{2}^- \rightarrow \frac{27}{2}^+$	20	5.17(16)	0.059(9)	0.79(17)	2256.9
806.3	$\frac{23}{2}^- \rightarrow \frac{21}{2}^+$	9	1.39(36)	0.020(7)	0.61(38)	1589.7
854.5	$\frac{27}{2}^- \rightarrow \frac{25}{2}^+$	27	0.63(27)	0.046(12)	0.91(27)	2063.2
821.5	$\frac{31}{2}^- \rightarrow \frac{29}{2}^+$	63	0.45(22)	0.083(18)	0.73(19)	2548.5
740.9	$\frac{35}{2}^- \rightarrow \frac{33}{2}^+$	67	1.05(12)	0.067(9)	0.81(14)	3067.0
654.6	$\frac{39}{2}^- \rightarrow \frac{37}{2}^+$	25	2.68(22)	0.066(15)	0.66(28)	3646.0
Band 3						
386.0	$\frac{15}{2}^- \rightarrow \frac{11}{2}^-$	20			1.70(71)	782.4
467.1	$\frac{19}{2}^- \rightarrow \frac{15}{2}^-$	29			1.15(32)	1249.5
534.2	$\frac{23}{2}^- \rightarrow \frac{19}{2}^-$	15			1.29(76)	1783.7
585.6	$\frac{27}{2}^- \rightarrow \frac{23}{2}^-$	$\cong 19$			1.96(54)	2369.3
611.0	$\frac{31}{2}^- \rightarrow \frac{27}{2}^-$	$\cong 16$			1.07(38)	2980.3
585.6	$\frac{35}{2}^- \rightarrow \frac{31}{2}^-$	$\leqslant 19$			1.96(54)	3565.9
428.2	$\frac{17}{2}^- \rightarrow \frac{13}{2}^-$	25			1.00(38)	1006.7
502.3	$\frac{21}{2}^- \rightarrow \frac{17}{2}^-$	25			1.13(44)	1509.0
562.0	$\frac{25}{2}^- \rightarrow \frac{21}{2}^-$	26			1.02(30)	2071.0
603.0	$\frac{29}{2}^- \rightarrow \frac{25}{2}^-$	21			1.52(49)	2674.0
182.1	$\frac{13}{2}^- \rightarrow \frac{11}{2}^-$	$\cong 78$			0.55(11)	578.5
204.0	$\frac{15}{2}^- \rightarrow \frac{13}{2}^-$	50			0.74(13)	782.4
224.1	$\frac{17}{2}^- \rightarrow \frac{15}{2}^-$	31			0.75(15)	1006.7
242.7	$\frac{19}{2}^- \rightarrow \frac{17}{2}^-$	21			0.37(35)	1249.5
259.7	$\frac{21}{2}^- \rightarrow \frac{19}{2}^-$	9			0.87(29)	1509.0
274.5	$\frac{23}{2}^- \rightarrow \frac{21}{2}^-$	8			0.73(25)	1783.7
287.4	$\frac{25}{2}^- \rightarrow \frac{23}{2}^-$	10			0.65(19)	2071.0
297.5	$\frac{27}{2}^- \rightarrow \frac{25}{2}^-$	4			0.44(14)	2369.3
305.0	$\frac{29}{2}^- \rightarrow \frac{27}{2}^-$	$\cong 5$			0.79(30)	2674.0
306.0	$\frac{31}{2}^- \rightarrow \frac{29}{2}^-$	$\cong 5$			0.79(30)	2980.3

[a]Uncertainties between 0.1 and 0.5 keV.
[b]See text for details about the spin and parity assignments.
[c]Uncertainties between 5% and 30%. Normalized to the 198.7-keV transition.
[d]Branching ratio, $T_\gamma(I \rightarrow I-2)/T_\gamma(I \rightarrow I-1)$. $T_\gamma(I \rightarrow I-2)$ and $T_\gamma(I \rightarrow I-1)$ are the relative γ intensities of the $E2$ and $E1$ transitions depopulating the level I, respectively.
[e]Exciton energies of the initial states.

transform the experimental excitation energies and spins into the rotating frame [35]. The standard plot of the aligned angular momentum (i) for each band observed in ^{161}Er as a function of rotational frequency is shown in Fig. 5. These quantities are extracted from the measured spins, level energies, and transition energies according to Ref. [35]. The quasiparticle aligned angular momentum results from the subtraction of reference angular momentum, $\omega J_0 + \omega^3 J_1$, from the total angular momentum along the rotational axis. The Harris parameters $J_0 = 26.0$ MeV^{-1} and $J_1 = 90.0$ MeV^{-3} are used [35], which give a nearly constant alignment for the $(\pi, \alpha) = (+, +\frac{1}{2})$ sequence in ^{161}Er before the first band crossing and zero alignment for the ground-state bands of the neighboring even-even nuclei ^{160}Er and ^{162}Er [36,37]. For comparison, the alignment for the yrast band of ^{162}Er is also presented in Fig. 5. Some interesting experimental results are given below.

In band 1, the two signature branches show rather large initial alignments of $4.5\hbar$ and $4.0\hbar$, and experience a pronounced upbend at $\hbar\omega \approx 0.37$ MeV. The band crossings could be interpreted as the neutron BC and AD alignments [35–37].

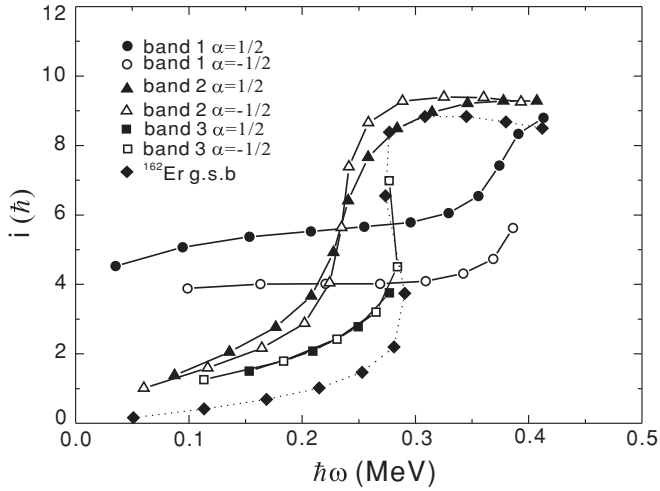

FIG. 5. Extracted alignment for bands in ^{161}Er. The labels in the legends indicate the bands as they are labeled in Fig. 1. The Harris reference parameters are chosen to be $J_0 = 26.0$ MeV^{-1} and $J_1 = 90.0$ MeV^{-3}. The alignment for the yrast band of ^{162}Er is also shown for comparison.

In band 2, the two signature branches behave similarly, and band crossing takes place at $\hbar\omega \approx 0.24$ MeV. This band shows a total alignment gain of about $7.0\hbar$ after the crossing, which is consistent with the $i_{13/2}$ neutron alignment [36,37]. The band crossing frequency is about 40 keV lower than that of the yrast band in the neighboring even-even nucleus ^{162}Er [37]. This phenomenon was observed in a number of odd-A nuclei in the rare-earth region, and it could be explained by a reduction of neutron pairing correlation [38]. One interesting feature here is that the alignment curves for the two signature branches cross at $\hbar\omega \approx 0.24$ MeV as shown in Fig. 5. This indicates that signature inversion occurs after the band crossing in band 2.

In band 3, the two signatures show almost identical behavior up to the highest state observed. With addition of two transitions on the top of band 3, a band crossing at $\hbar\omega \approx 0.28$ MeV is observed for the first time. The alignment gain could not be deduced in the present work because the crossing is not yet completed at the last transition observed. The band-crossing frequency is nearly equal to that for the yrast band in ^{162}Er [37], and therefore the band crossing is attributed to the neutron AB alignment.

B. Signature splitting properties

Bands 1 and 2 display large signature splitting in the whole spin region observed experimentally. The signature splitting Δe is defined as the difference in energies at a given rotational frequency for the pair of signature partners. Figures 6 and 7 present plots of the signature splitting for bands 1 and 2, defined as [39]

$$S(I) = [E(I) - E(I-1)] - \tfrac{1}{2}[E(I+1) - E(I) + E(I-1) - E(I-2)]. \quad (12)$$

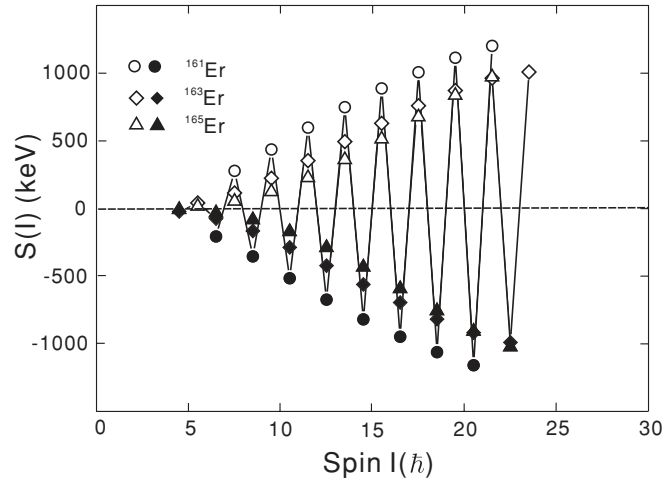

FIG. 6. Experimental signature splitting $S(I)$ for the $5/2^+[642]$ bands in ^{161,163,165}Er. The solid (open) symbols correspond to the levels with favored signature $\alpha_f = +\frac{1}{2}$ (unfavored signature $\alpha_{\rm uf} = -\frac{1}{2}$).

Here $E(I)$ is the level energy of state I; $S(I)$ is directly proportional to the signature splitting Δe, but magnified by approximately a factor of two.

The $5/2^+[642]$ configuration was assigned to band 1 [1,2]. As shown in Fig. 6, band 1 displays large energy splitting. For comparison, the signature splitting of the positive-parity band in the odd-A Er isotopes is also plotted in Fig. 6. It can be seen from this figure that the energy splitting decreases slightly with increasing N from ^{161}Er ($N = 93$) to ^{165}Er ($N = 97$) [3,5]. A similar trend was observed in the odd Yb and Dy isotopes with neutron numbers from 93 to 97 [7,40]. Signature splitting in energy is considered generally as a consequence of the mixing of the $\Omega = 1/2$ orbits into the wave functions from the Coriolis interaction. The neutron Fermi surface lies in the $i_{13/2}$ subshell, and it gradually approaches the $\Omega = 1/2$ orbit

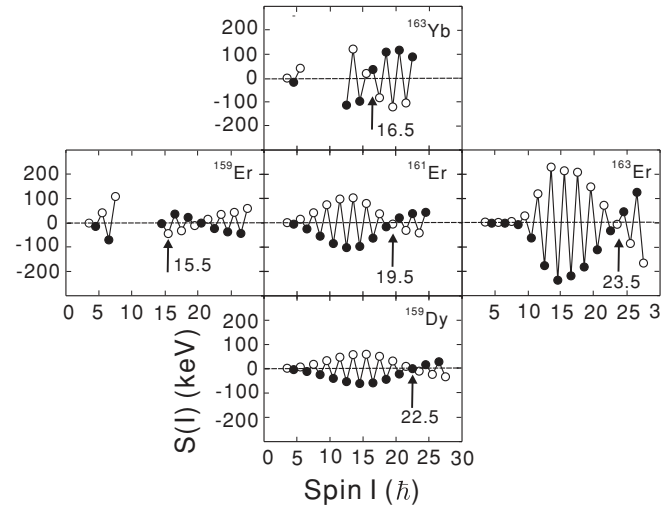

FIG. 7. Compilation of signature inversion for the $3/2^-[521]$ bands in ^{159,161,163}Er, ^{159}Dy, and ^{163}Yb. The solid (open) symbols correspond to the levels with favored signature $\alpha_f = +\frac{1}{2}$ (unfavored signature $\alpha_{\rm uf} = -\frac{1}{2}$). The arrows indicate the signature crossing spins.

while decreasing the neutron number. This could explain the very large energy signature splitting in the $5/2^+[642]$ band in ^{161}Er [7,40].

Band 2 was associated with the $3/2^-[521]$ ground state [1,2]. As shown in Fig. 7, band 2 displays increasing signature splitting with increasing angular momentum, and the splitting reaches a maximum at $I = 13.5\hbar$. At high-spin sates, the signature splitting decreases, and the two signature branches cross with each other at $I_c = 19.5\hbar$. Furthermore, the signature splitting increases again beyond the crossing point. Similar signature inversion phenomenon was observed in the $3/2^-[521]$ band in the ^{163}Yb [7] and ^{159}Dy [8] isotones, and the ^{159}Er [6] and ^{163}Er isotopes [3] of ^{161}Er. Therefore, it is necessary to systematically analyze the signature inversion phenomenon in this mass region. The level staggering curves for the $3/2^-[521]$ bands in the concerned nuclei are also presented in Fig. 7. From careful inspection of Fig. 7, one can draw the following conclusions. In the chain of isotone, the inversion point shifts to lower spin with increasing proton number; the crossing occurs at $I_c = 19.5\hbar$ in ^{161}Er, which is about three units higher/lower than that in ^{163}Yb/^{159}Dy. Additionally, the amplitude of signature splitting increases with increasing proton number. In the chain of isotope, the inversion point shifts to higher spin with increasing neutron number; the crossing spin increases four units once increasing two neutrons.

Different mechanisms have been proposed to interpret the signature inversion phenomenon observed in the $3/2^-[521]$ bands [6–8,40]. In the ^{163}Yb and ^{159}Dy isotones, the signature inversion was explained by a small change in deformation before and after the alignment of a pair of $i_{13/2}$ neutrons [7,8,40]. The signature inversion in ^{159}Er could not be reproduced theoretically if only the ε_2 and ε_4 deformations were included in the calculations [6], and it was suggested that a change in triaxial deformation induced by the $i_{13/2}$ neutron alignment might be the reason for the signature inversion [6]. There is a naive explanation of the signature inversion associated with the $3/2^-[521]$ bands in the odd-N nuclei. For a near-prolate deformation in this mass region, the $3/2^-[521]$ and $5/2^-[523]$ orbits lie close to the Fermi surface, and there may be some mixing between them. These two orbits originate from the $h_{9/2}$ and $f_{7/2}$ shell-model parentages, respectively. The favored signature for the $3/2^-[521]$ and $5/2^-[523]$ orbits has the opposite value. Therefore, signature inversion could occur if the low-lying states have a dominant $3/2^-[521]$ configuration, while the main component of the wave functions for the high-lying states becomes the $5/2^-[523]$ configuration.

To have a deeper understanding of the band properties in ^{161}Er, we have performed the calculations based on the PRM [31]. In the present calculations, we set the ε_2, ε_4, and ε_6 deformation parameters to be 0.242, −0.020, and 0.010 according to Ref. [41]. Standard values for κ and μ strengths in the $\vec{l}\cdot\vec{s}$ and $\vec{l}^2$ terms are used, and an off-diagonal Coriolis attenuation parameter $\xi = 0.75$ is adopted [33,34]. The moment of inertia $\Im_0$ is obtained for the negative-parity band from the slope of the level energy versus spin curve in the neighboring even-even Er nuclei, and a variable moment of inertia is used for the positive-parity band to reproduce the experimental energy spectrum. The neutron Fermi energy λ_n is taken to be the energy of the single-particle level occupied by the last neutron. Pairing correlations are treated via a standard BCS approximation using values of $G_0 = 19.2$ MeV and $G_1 = 7.4$ MeV [42]. The triaxiality γ is adjusted to fit the experimental level energies.

In the PRM calculation, we take orbits near the Fermi surface coupled to a triaxial-rotor core. The experimental level energies are fitted with the calculated results by varying the value of triaxiality. It is found that the level energy $E(I)$ can be best reproduced when setting $\gamma = -2^\circ$ and 12° for the yrast positive-parity and negative-parity bands, respectively. Fixing $\gamma = -2^\circ$ and 12°, the single-particle Hamiltonian is diagonalized, and the main components of the single-particle orbits near the Fermi surface in terms of the deformed Nilsson levels are obtained. The results for six positive-parity orbits and six negative-parity orbits are listed in Table II. In a triaxially deformed potential, the number ν is adopted to denote the single-particle state according to the sequence in energy. For convenience, the Nilsson orbit is also used to indicate the

TABLE II. Positive-parity and negative-parity single-particle levels $|\nu\rangle$ at $\gamma = -2^\circ$ and 12°, respectively. The approximate Nilsson quantum numbers, single-particle energies, and main components expanded in the basis $|Nlj\Omega\rangle$, are shown. The neutron Fermi energy λ_n is 51.47 MeV at $\gamma = -2^\circ$ and 51.48 MeV at $\gamma = 12^\circ$.

γ	$\lvert\nu\rangle$	$\Omega^\pi[Nn_z\Lambda]$	ϵ_ν(MeV)	Main components in terms of $\lvert Nlj\Omega\rangle$
	$\lvert 23\rangle$	$1/2^+[660]$	50.54	$-0.857\lvert 6i_{13/2}1/2\rangle - 0.462\lvert 6g_{9/2}1/2\rangle - 0.193\lvert 6d_{5/2}1/2\rangle$
	$\lvert 24\rangle$	$3/2^+[651]$	51.14	$-0.895\lvert 6i_{13/2}-3/2\rangle - 0.410\lvert 6g_{9/2}-3/2\rangle - 0.124\lvert 6d_{5/2}-3/2\rangle$
	$\lvert 25\rangle$	$5/2^+[642]$	52.16	$-0.939\lvert 6i_{13/2}5/2\rangle - 0.323\lvert 6g_{9/2}5/2\rangle - 0.053\lvert 6d_{5/2}5/2\rangle$
-2°	$\lvert 26\rangle$	$7/2^+[633]$	53.51	$0.971\lvert 6i_{13/2}-7/2\rangle + 0.217\lvert 6g_{9/2}-7/2\rangle + 0.092\lvert 6i_{11/2}-7/2\rangle$
	$\lvert 27\rangle$	$1/2^+[631]$	54.95	$0.543\lvert 6d_{5/2}1/2\rangle + 0.483\lvert 6g_{9/2}1/2\rangle + 0.430\lvert 6i_{13/2}1/2\rangle$
	$\lvert 28\rangle$	$9/2^+[624]$	55.07	$-0.990\lvert 6i_{13/2}9/2\rangle - 0.112\lvert 6g_{9/2}9/2\rangle + 0.081\lvert 6i_{11/2}9/2\rangle$
	$\lvert 21\rangle$	$11/2^-[505]$	50.24	$0.994\lvert 5h_{11/2}-11/2\rangle - 0.106\lvert 5f_{7/2}-7/2\rangle$
	$\lvert 22\rangle$	$3/2^-[532]$	50.27	$-0.592\lvert 5h_{9/2}-3/2\rangle - 0.378\lvert 5f_{7/2}-3/2\rangle - 0.324\lvert 5f_{5/2}-3/2\rangle$
	$\lvert 23\rangle$	$3/2^-[521]$	51.25	$0.676\lvert 5f_{7/2}-3/2\rangle - 0.559\lvert 5h_{9/2}-3/2\rangle - 0.217\lvert 5h_{11/2}-3/2\rangle$
12°	$\lvert 24\rangle$	$5/2^-[523]$	51.80	$0.811\lvert 5h_{9/2}5/2\rangle - 0.374\lvert 5f_{7/2}5/2\rangle + 0.199\lvert 5f_{5/2}5/2\rangle$
	$\lvert 25\rangle$	$5/2^-[512]$	53.16	$-0.736\lvert 5f_{7/2}5/2\rangle - 0.506\lvert 5h_{9/2}5/2\rangle + 0.257\lvert 5p_{3/2}1/2\rangle$
	$\lvert 26\rangle$	$1/2^-[521]$	53.22	$0.460\lvert 5f_{5/2}1/2\rangle - 0.435\lvert 5h_{9/2}1/2\rangle - 0.403\lvert 5p_{1/2}1/2\rangle$

main component of the single-particle state in Table II. The total wave functions for the selected states in bands 1 and 2, expanded in the strong coupling basis $|IMK\nu\rangle$, are shown in Table III.

As shown in Fig. 8, the level energy $E(I)$ and signature splitting $S(I)$ for band 1 are reproduced excellently well when setting $\gamma = -2^\circ$. This could strongly suggest that band 1 exhibits a near-prolate deformation. The neutron Fermi surface λ_n is determined to be 51.47 MeV at $\gamma = -2^\circ$. Inspecting Table III, we can recognize that, in spite of the strong mixing among the 23th, 24th, 25th, and 26th orbits from the Coriolis interaction, band 1 arises mainly from the $i_{13/2}$ subshell. As the angular momentum increases, the mixing of the $\Omega = 1/2$ component into the wave functions gradually increases because of the large Coriolis interaction. This could explain the pattern of signature splitting shown in Fig. 6.

For the yrast negative-parity band, the variation of the signature splitting before the band crossing against the triaxiality is investigated, and the calculated results for $\gamma = 0^\circ$ and 12° are presented in Fig. 9. At a prolate deformation ($\gamma = 0^\circ$), no signature splitting would be observed because the valence neutron should mainly occupy the $3/2^-[521]$ Nilsson orbit. While increasing the triaxiality value, the calculated signature splitting becomes larger and larger. The experimental level energy and signature splitting in band 2 can be best reproduced theoretically while assuming $\gamma = 12^\circ$. This would suggest that band 2 has a triaxial deformation. As shown in Table III, the wave functions of the states before the band crossing in band 2 are dominated by the orbits originated from the $h_{9/2}$ subshell, and therefore the $\alpha = 1/2$ sequence is favored in energy. Meanwhile, it is interesting to note that the low-lying states have a strong mixture of configurations having the

TABLE III. Main components expanded in the strong coupling basis $|IMK\nu\rangle$ (denoted as $|K\nu\rangle$ for short) for selected states in the $5/2^+[642]$ band and $3/2^-[521]$ band.

I^π	Main components in terms of $\lvert K\nu\rangle$
$9/2^+$	$-0.586\lvert 1/2\ 23\rangle - 0.661\lvert -3/2\ 24\rangle - 0.456\lvert 5/2\ 25\rangle$
$11/2^+$	$-0.194\lvert 1/2\ 23\rangle + 0.676\lvert -3/2\ 24\rangle - 0.685\lvert 5/2\ 25\rangle$
$13/2^+$	$0.637\lvert 1/2\ 23\rangle + 0.632\lvert -3/2\ 24\rangle + 0.422\lvert 5/2\ 25\rangle$
$15/2^+$	$0.662\lvert 1/2\ 24\rangle - 0.683\lvert 5/2\ 25\rangle - 0.226\lvert -7/2\ 26\rangle$
$17/2^+$	$-0.665\lvert 1/2\ 23\rangle - 0.615\lvert -3/224\rangle - 0.401\lvert 5/2\ 25\rangle$
$19/2^+$	$-0.653\lvert 1/2\ 24\rangle + 0.680\lvert 5/2\ 25\rangle + 0.254\lvert -7/2\ 26\rangle$
$21/2^+$	$-0.683\lvert 1/2\ 23\rangle - 0.603\lvert -3/224\rangle - 0.386\lvert 5/2\ 25\rangle$
$23/2^+$	$-0.647\lvert 1/2\ 24\rangle + 0.678\lvert 5/2\ 25\rangle + 0.274\lvert -7/2\ 26\rangle$
$25/2^+$	$-0.696\lvert 1/2\ 23\rangle - 0.595\lvert -3/224\rangle - 0.374\lvert 5/2\ 25\rangle$
$27/2^+$	$-0.642\lvert 1/2\ 24\rangle + 0.675\lvert 5/2\ 25\rangle + 0.288\lvert -7/2\ 26\rangle$
$29/2^+$	$-0.705\lvert 1/2\ 23\rangle - 0.589\lvert -3/224\rangle - 0.366\lvert 5/2\ 25\rangle$
$31/2^+$	$0.638\lvert 1/2\ 24\rangle - 0.672\lvert 5/2\ 25\rangle - 0.299\lvert -7/2\ 26\rangle$
$33/2^+$	$0.713\lvert 1/2\ 23\rangle + 0.584\lvert -3/224\rangle + 0.359\lvert 5/2\ 25\rangle$
$35/2^+$	$0.635\lvert 1/2\ 24\rangle - 0.670\lvert 5/2\ 25\rangle - 0.308\lvert -7/2\ 26\rangle$
$37/2^+$	$0.718\lvert 1/2\ 23\rangle + 0.580\lvert -3/224\rangle + 0.353\lvert 5/2\ 25\rangle$
$39/2^+$	$0.633\lvert 1/2\ 24\rangle - 0.669\lvert 5/2\ 25\rangle - 0.315\lvert -7/2\ 26\rangle$
$41/2^+$	$-0.723\lvert 1/2\ 23\rangle - 0.577\lvert -3/224\rangle - 0.348\lvert 5/2\ 25\rangle$
$3/2^-$	$-0.982\lvert -3/2\ 23\rangle - 0.177\lvert -3/2\ 24\rangle$
$5/2^-$	$-0.675\lvert -3/2\ 23\rangle + 0.706\lvert 5/2\ 24\rangle + 0.126\lvert 5/2\ 23\rangle - 0.123\lvert -3/2\ 24\rangle$
$7/2^-$	$-0.699\lvert -3/2\ 23\rangle - 0.678\lvert 5/2\ 24\rangle - 0.128\lvert 5/2\ 24\rangle + 0.121\lvert 5/2\ 23\rangle$
$9/2^-$	$-0.701\lvert -3/2\ 23\rangle + 0.665\lvert 5/2\ 24\rangle - 0.129\lvert -3/2\ 24\rangle - 0.119\lvert 5/2\ 23\rangle$
$11/2^-$	$0.719\lvert -3/2\ 23\rangle + 0.642\lvert 5/2\ 24\rangle - 0.141\lvert 5/2\ 25\rangle + 0.134\lvert -3/2\ 24\rangle$
$13/2^-$	$-0.700\lvert -3/2\ 23\rangle + 0.638\lvert 5/2\ 24\rangle - 0.153\lvert 5/2\ 25\rangle - 0.130\lvert -3/2\ 24\rangle$
$15/2^-$	$0.730\lvert -3/2\ 23\rangle + 0.610\lvert 5/2\ 24\rangle - 0.175\lvert 5/2\ 25\rangle + 0.138\lvert -3/2\ 24\rangle$
$17/2^-$	$-0.685\lvert -3/2\ 23\rangle + 0.612\lvert 5/2\ 24\rangle - 0.175\lvert 5/2\ 25\rangle + 0.157\lvert 1/2\ 23\rangle$
$19/2^-$	$-0.737\lvert -3/2\ 23\rangle - 0.576\lvert 5/2\ 24\rangle + 0.202\lvert 5/2\ 25\rangle - 0.143\lvert -3/2\ 24\rangle$
$21/2^-$	$-0.661\lvert -3/2\ 23\rangle + 0.584\lvert 5/2\ 24\rangle + 0.214\lvert 1/2\ 23\rangle - 0.186\lvert 5/2\ 25\rangle$
$23/2^-$	$0.739\lvert -3/2\ 23\rangle + 0.537\lvert 5/2\ 24\rangle - 0.222\lvert 5/2\ 25\rangle + 0.147\lvert -3/2\ 24\rangle$
$25/2^-$	$-0.634\lvert -3/2\ 23\rangle + 0.554\lvert 5/224\rangle + 0.262\lvert 1/2\ 23\rangle - 0.190\lvert 5/2\ 25\rangle$
$27/2^-$	$0.733\lvert -3/2\ 23\rangle + 0.495\lvert 5/2\ 24\rangle - 0.235\lvert 5/2\ 25\rangle - 0.190\lvert 1/2\ 23\rangle$
$29/2^-$	$-0.607\lvert -3/2\ 23\rangle + 0.524\lvert 5/2\ 24\rangle + 0.300\lvert 1/2\ 23\rangle - 0.190\lvert 5/2\ 25\rangle$
$31/2^-$	$-0.720\lvert -3/2\ 23\rangle - 0.455\lvert 5/224\rangle + 0.242\lvert 5/2\ 25\rangle + 0.234\lvert 1/2\ 23\rangle$
$33/2^-$	$-0.583\lvert -3/2\ 23\rangle + 0.496\lvert 5/2\ 24\rangle + 0.329\lvert 1/2\ 23\rangle - 0.188\lvert 5/2\ 25\rangle$
$35/2^-$	$-0.702\lvert -3/2\ 23\rangle - 0.419\lvert 5/2\ 24\rangle + 0.271\lvert 1/2\ 23\rangle + 0.259\lvert -7/2\ 23\rangle$
$37/2^-$	$0.562\lvert -3/2\ 23\rangle - 0.470\lvert 5/224\rangle - 0.349\lvert 5/2\ 23\rangle - 0.202\lvert 1/2\ 23\rangle$
$39/2^-$	$0.682\lvert -3/2\ 23\rangle + 0.391\lvert 5/224\rangle - 0.300\lvert 1/2\ 23\rangle - 0.288\lvert -7/2\ 23\rangle$
$41/2^-$	$0.544\lvert -3/2\ 23\rangle - 0.447\lvert 5/224\rangle - 0.363\lvert 1/2\ 23\rangle - 0.220\lvert -7/2\ 23\rangle$

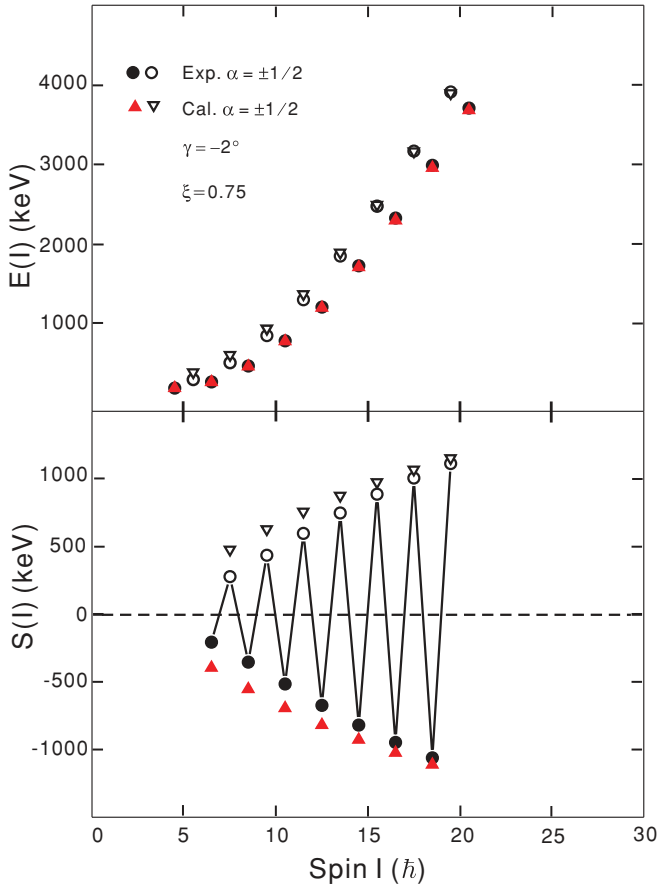

FIG. 8. (Color online) Energy spectrum $E(I)$ and signature splitting $S(I)$ for the $5/2^+[642]$ band calculated by the PRM in comparison with the experimental data.

parentages of $h_{9/2}$ and $f_{7/2}$. It is eagerly desired to know the wave functions of the high-lying states in band 2 to understand the signature inversion observed experimentally. However, the self-consistent explanation of signature inversion in band 2 is beyond the present one quasineutron coupled with a triaxially deformed core.

C. The enhanced $E1$ transitions

In the present work, the strong $E1$ transitions from the $3/2^-[521]$ band to the $5/2^+[642]$ band have been observed in ^{161}Er. In fact, the occurrence of relatively enhanced $E1$ transitions is a general phenomenon in the rare-earth region, and enhanced $E1$ transitions between two bands with opposite parities are observed in a batch of odd-A nuclei [3,5,7,8,11]. In a model of one quasiparticle coupled to an axially symmetric rotor [9–11], the calculated $B(E1)$ values are at least one order of magnitude smaller than the experimental ones. Because the measured magnitudes of $B(E1)$ values could not be reproduced with the standard $E1$ transition operator, the following $E1$ transition operator effectively taking into account the octupole softness was proposed [9–11]:

$$O(E1,\nu) = e_{\rm eff}(E1) r Y_{1\nu} + e b_\nu r^3 Y_{3\nu}. \tag{13}$$

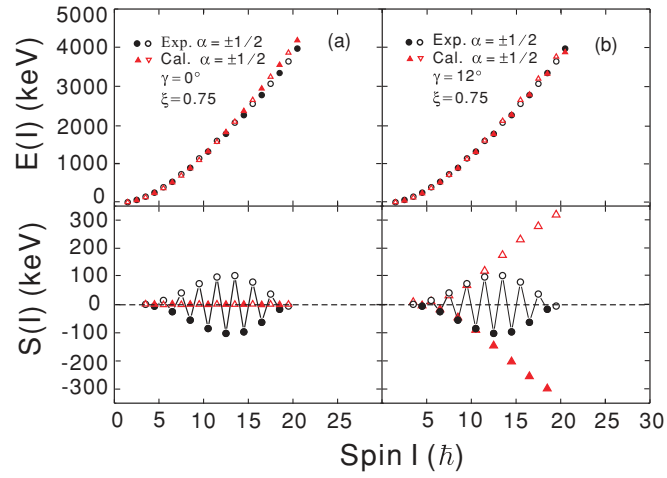

FIG. 9. (Color online) Energy spectrum $E(I)$ and signature splitting $S(I)$ for the $3/2^-[521]$ band calculated by the PRM in comparison with the experimental data.

The second term on the right-hand side of Eq. (13) can cause an enhancement of the $E1$ transition strength. The experimental $B(E1)$ values observed in the odd-A rare-earth nuclei were analyzed in terms of b_ν parameters [9–11], which effectively express the effect of octupole vibrations on the $E1$ transitions. If the parameters b_0 and $b_{\pm1}$ were chosen properly, a satisfactory agreement between the measured and calculated $B(E1)$ values can be obtained [9–11]. However, the b_ν values depend on nuclei, and are sensitive to pairs of bands studied [10,11]. Furthermore, the b_ν values necessary for reproducing experimental data could not be obtained using microscopic models [10,11].

The intensity relation for electromagnetic transition rates is a powerful tool to probe the properties of nuclear collective motions. The intensity ratios $B(E1)/B(E2)$ between the intraband $E2$ transition and interband $E1$ transition in ^{161}Er are deduced according to the prescription given in Sec. II, and listed in Table II. The $B(E1)/B(E2)$ ratios are comparable with those observed in neighboring nuclei [3,7,8,11]. In the present work, the cranking formalism of the generalized intensity relation is adopted to study the enhanced $E1$ transitions in ^{161}Er [8,12,40,43,44]. In the rotational model, the intensity ratio $B(E1)/B(E2)$ can be related with the quantity $R(E1/E2)$, defined as [40]

$$\begin{aligned} R(E1/E2) &\equiv \left[\frac{B(E1;K_i, I \to K_f, I-1)}{B(E2;K_i, I \to K_i, I-2)}\right]^{1/2} \\ &\quad \times \left|\frac{\langle I, K_i, 2, 0 | I-2, K_i\rangle}{\langle I, K_i, 1, 1 | I-1, K_f\rangle}\right| \\ &= \frac{1}{\sqrt{5/16\pi}\, Q_0}\{M_1 + M_2[I_f(I_f+1) \\ &\quad - I_i(I_i+1)]\}. \end{aligned} \tag{14}$$

Here, M_1 and M_2 are the I-independent and leading order I-dependent intrinsic $E1$ matrix elements, respectively [40]. The value of M_2 reflects the Coriolis interaction or the probable contribution from the octupole correlation [12]. Q_0 is the intrinsic quadrupole moment of the band associated

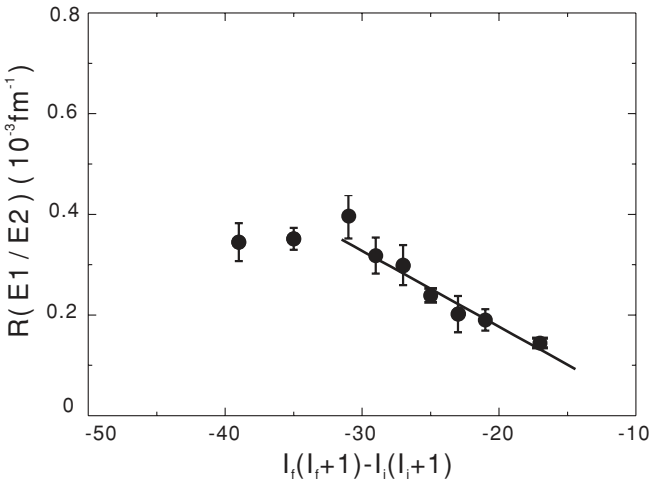

FIG. 10. Experimental $R(E1/E2)$ ratios as a function of $I_f(I_f + 1) - I_i(I_i + 1)$ for the $3/2^-[521]$ band. The straight line is obtained by the least-square fit to the six data points before the band crossing.

with K_i [40]. For the $E1$ transitions from the $3/2^-[521]$ band to the $5/2^+[642]$ band in ^{161}Er, K_i and K_f are equal to $3/2$ and $5/2$, respectively. The value of $Q_0 = 7.01eb$ is used [2]. The experimental values of $R(E1/E2)$ versus $I_f(I_f + 1) - I_i(I_i + 1)$ are shown in Fig. 10. The values of $R(E1/E2)$ show pronounced angular momentum dependence. The M_1 and M_2 parameters are deduced to be $-0.000\,276$ and $-0.000\,033$ by fitting the data points before the band crossing with a straight line. It is interesting to note that the parameter M_2 is not equal to zero. Therefore, there is a substantial mixing between the initial and final states. The admixture might result from the octupole correlation [9].

V. SUMMARY

The well-deformed nucleus ^{161}Er was produced in the bombardment of the ^{150}Nd target with the ^{16}O projectiles. The previously known rotational bands based on the $5/2^+[642]$, $3/2^-[521]$, and $11/2^-[505]$ configurations have been extended up to $53/2^+$, $53/2^-$, and $35/2^-$ states, respectively. The $\alpha = -1/2$ branch of the ground-state $3/2^-[521]$ band is revised significantly. Importantly, nine relatively enhanced $E1$ transitions from the negative-parity $3/2^-[521]$ band to the positive-parity $5/2^+[642]$ band are observed. The properties of bands associated with the $5/2^+[642]$ and $3/2^-[521]$ configurations are analyzed using the triaxial particle-rotor model. The level energy and large signature splitting in the $5/2^+[642]$ band can be well reproduced by the PRM calculation if assuming a near-prolate deformation. The $3/2^-[521]$ band experiences a band crossing at $\hbar\omega \approx 0.24$ MeV, and it is attributed to the $i_{13/2}$ neutron alignment. The signature splitting before the band crossing would be caused by the triaxial deformation. It was observed that the signature splitting is inverted after the band crossing in the $3/2^-[521]$ band. The systematics of the signature inversion associated with the $3/2^-[521]$ configuration are presented. The spin value of the inversion point shows a very regular pattern while changing proton or neutron numbers, and this phenomenon is deserving of theoretical study. The neutron AB crossing was observed at $\hbar\omega \approx 0.28$ MeV for the first time in the $11/2^-[505]$ band. The properties of the enhanced $E1$ transitions have been discussed on the base of the generalized intensity relation. The $R(E1/E2)$ values show pronounced angular momentum dependence before the band crossing, and the relatively enhanced $E1$ transitions could be attributed to octupole softness.

ACKNOWLEDGMENTS

The authors are grateful to the staff of the in-beam γ-ray group and the tandem accelerator group at China Institute of Atomic Energy for their help. This work was supported by the National Natural Science Foundation of China (Grant Nos. 10825522, 10735010, and 10575120), the National Basic Research Program of China (Grant No. 2007CB815001), and the Chinese Academy of Sciences.

[1] J. D. Garrett *et al.*, Phys. Lett. B **118**, 297 (1982).
[2] S. A. Hjorth *et al.*, Nucl. Phys. A **144**, 513 (1970).
[3] G. B. Hagemann *et al.*, Nucl. Phys. A **618**, 199 (1997).
[4] A. Brockstedt *et al.*, Nucl. Phys. A **571**, 337 (1994).
[5] S. T. Wang *et al.*, Chin. Phys. C **33**, 629 (2009).
[6] J. Simpson *et al.*, J. Phys. G **10**, 383 (1984).
[7] J. Kownacki *et al.*, Nucl. Phys. A **394**, 269 (1983).
[8] M. Sugawara *et al.*, Nucl. Phys. A **699**, 450 (2002).
[9] I. Hamamoto *et al.*, Phys. Lett. B **226**, 17 (1989).
[10] I. Hamamoto, Nucl. Phys. A **557**, 515c (1993).
[11] G. B. Hagemann, I. Hamamoto, and W. Satuła, Phys. Rev. C **47**, 2008 (1993).
[12] A. Bohr and B. R. Mottelson, *Nuclear Structure* (Benjamin, New York, 1975), Vol. 2.
[13] R. Bengtsson, H. Frisk, and F. R. May, Nucl. Phys. A **415**, 189 (1984).
[14] D. J. Hartley *et al.*, Phys. Rev. C **58**, 2720 (1998).
[15] O. Zeidan *et al.*, Phys. Rev. C **65**, 024303 (2002).
[16] A. Ikeda and T. Shimano, Phys. Rev. Lett. **63**, 139 (1989).
[17] I. Hamamoto and H. Sagawa, Phys. Lett. B **201**, 415 (1988).
[18] P. A. Butler and W. Nazarewicz, Rev. Mod. Phys. **68**, 349 (1996).
[19] V. M. Strutinsky, J. Nucl. Energy **4**, 523 (1957).
[20] A. Bohr and B. R. Mottelson, Nucl. Phys. **4**, 529 (1957); **9**, 687 (1958-1959).
[21] M. Gai *et al.*, Phys. Rev. Lett. **51**, 646 (1983).
[22] D. Ward *et al.*, Nucl. Phys. A **406**, 591 (1983).
[23] W. Nazarewicz and S. L. Tabor, Phys. Rev. C **45**, 2226 (1992).
[24] W. R. Phillips, I. Ahmad, H. Emling, R. Holzmann, R. V. F. Janssens, T. L. Khoo, and M. W. Drigert, Phys. Rev. Lett. **57**, 3257 (1986).
[25] T. Hayakawa *et al.*, Phys. Lett. B **551**, 79 (2003).
[26] C. W. Reich and R. G. Helmer, Nucl. Data Sheets **90**, 645 (2000).
[27] J. Simpson *et al.*, Phys. Rev. C **62**, 024321 (2000).
[28] M. A. Riley *et al.*, J. Phys. G **16**, L67 (1990).

[29] J. Konijn *et al.*, Nucl. Phys. A **373**, 397 (1982).
[30] R. S. Guo and L. M. Chen, J. Phys. G **26**, 1775 (2000).
[31] B. Qi *et al.*, Int. J. Mod. Phys. E **18**, 109 (2009).
[32] J. Meyer-ter-vehn, Nucl. Phys. A **249**, 111 (1975).
[33] I. Ragnarsson and P. B. Semmes, Hyperfine Interact. **43**, 423 (1988).
[34] T. Bengtsson and I. Ragnarsson, Nucl. Phys. A **436**, 14 (1985).
[35] R. Bengtsson and S. Frauendorf, Nucl. Phys. A **327**, 139 (1979).
[36] J. Simpson *et al.*, J. Phys. G **13**, 847 (1987).
[37] H. Ryde, Acta Phys. Pol. B **27**, 15 (1996).
[38] J. D. Garrett *et al.*, Phys. Rev. Lett. **47**, 75 (1981).
[39] Y. H. Zhang *et al.*, Phys. Rev. C **65**, 014302 (2001).
[40] A. Jungclaus *et al.*, Phys. Rev. C **67**, 034302 (2003).
[41] P. Möller *et al.*, At. Data Nucl. Data Tables **59**, 185 (1995).
[42] P. Semmes and I. Ragnarsson, *The Particle Plus Triaxial Model: A User's Guide*, distributed at the Hands-On Nuclear Physics Workshop, Oak Ridge, TN, 5–16 August 1991 (unpublished).
[43] Y. R. Shimizu and T. Nakatsukasa, Nucl. Phys. A **611**, 22 (1996).
[44] D. Ward *et al.*, Nucl. Phys. A **600**, 88 (1996).